AIP | Review of Scientific Instruments

The unfolding of multichord Doppler spectrometry

N. J. Conway, P. G. Carolan, and M. R. Tournianski

Citation: Rev. Sci. Instrum. **70**, 934 (1999); doi: 10.1063/1.1149471
View online: http://dx.doi.org/10.1063/1.1149471
View Table of Contents: http://rsi.aip.org/resource/1/RSINAK/v70/i1
Published by the American Institute of Physics.

Related Articles

Fourier transform infrared absorption spectroscopy characterization of gaseous atmospheric pressure plasmas with 2 mm spatial resolution
Rev. Sci. Instrum. 83, 103508 (2012)

Kr II laser-induced fluorescence for measuring plasma acceleration
Rev. Sci. Instrum. 83, 103111 (2012)

Laser schlieren deflectometry for temperature analysis of filamentary non-thermal atmospheric pressure plasma
Rev. Sci. Instrum. 83, 103506 (2012)

Reconstruction of polar magnetic field from single axis tomography of Faraday rotation in plasmas
Phys. Plasmas 19, 103107 (2012)

Study of the plasma wave excited by intense femtosecond laser pulses in a dielectric capillary
Phys. Plasmas 19, 093121 (2012)

Additional information on Rev. Sci. Instrum.

Journal Homepage: http://rsi.aip.org
Journal Information: http://rsi.aip.org/about/about_the_journal
Top downloads: http://rsi.aip.org/features/most_downloaded
Information for Authors: http://rsi.aip.org/authors

ADVERTISEMENT

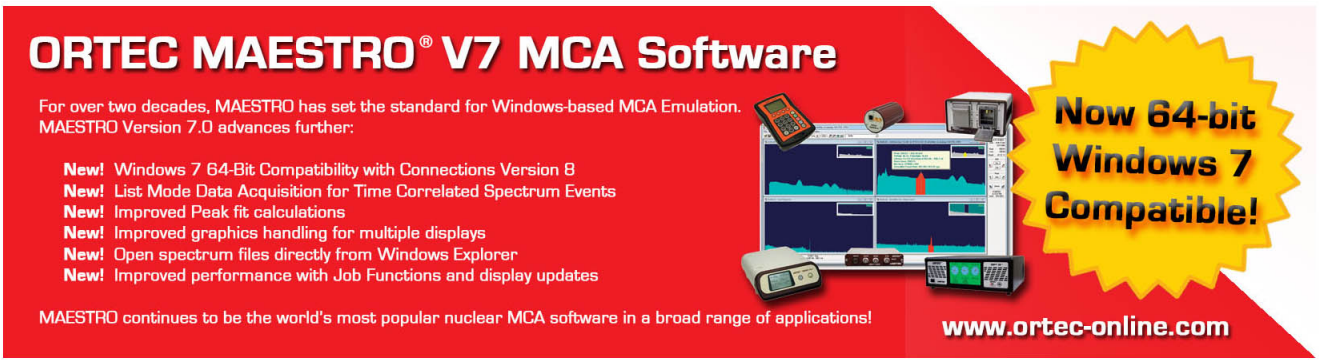

The unfolding of multichord Doppler spectrometry

N. J. Conway, P. G. Carolan, and M. R. Tournianski[a)]
EURATOM/UKAEA Fusion Association, Culham Science Centre, Abingdon, OX14 3DB, United Kingdom

(Presented on 10 June 1998)

A 20-chord Doppler spectrometer is used on the START spherical tokamak to record charge-exchange recombination (CXR) spectra (C^{5+} 5291 Å, $n=8\rightarrow7$). ''Passive'' radiation, mostly from near the plasma edge, is also present, and comes from electron-impact excitation of C^{5+} as well as C^{6+} CXR due to thermal neutrals. The relatively wide neutral beam, together with the blending of the passive and active emission, present difficult unfolding problems. These are overcome by imposing physics constraints such as constant ion temperatures on equilibrium magnetic flux surfaces. It is also necessary to model the beam-neutral atom density throughout the viewed equatorial plane. A nonlinear least-squares fitting code, using suitable profile parametrization, gives unfolded $T_i(r)$ and $v_\phi(r)$ profiles. These are presented along with estimates of the errors on the profiles. © *1999 American Institute of Physics.* [S0034-6748(99)69801-X]

I. INTRODUCTION

The START spherical tokamak[1,2] has neutral beam injection (NBI) heating which has assisted in the achievement of record beta values (~40%). The beam is also exploited by a charge-exchange diagnostic which measures ion temperature and toroidal velocity profiles. These complement the Thomson scattering measurements[3] of T_e and n_e profiles. The profiles are used in the investigation of ion heating and confinement and also overall plasma confinement.

The diagnostic measures charge-exchange line spectra from 20 lines of sight simultaneously in the plasma midplane. Because the neutral beam has a large diameter (roughly equal to the plasma minor radius) and is oriented tangentially, each line of sight collects light from an extended region of the plasma. This fact, combined with the presence of passive radiation (see below), necessitates an unfolding process to extract radial profiles from the spectra. (Strictly speaking, the procedure used involves a best-fit optimization for model functions, rather than a direct deconvolution or unfolding.)

II. APPARATUS

The orientation of the 20 lines of sight with respect to the neutral beam is shown in Fig. 1. Two collection heads are used, each holding ten sets of optical fibers. Each line of sight uses four 400 μm fibers in a linear bundle, offering cost and spatial resolution advantages compared to a single larger fiber.

The collection lenses, spectrometer and detector system are described in detail in Refs. 4 and 5, but to summarize: the full set of 20 lines of sight are linked to a 1 m Czerny–Turner spectrometer with a 2400 groove/mm holographic grating, coupled to a single CCD camera. A two-dimensional slit array is used (5×4), in conjunction with a narrowband interference filter which prevents slit-to-slit spectral crosstalk.

The instrument typically operates with a 2 ms integration period.

III. EXPERIMENTAL DATA

After a detailed survey of various possible charge-exchange lines, the carbon line at 5291 Å was chosen (this line is widely used on other tokamaks), as the spectral region was reasonably free from interfering emission lines.

On START, as in other tokamaks (e.g., ASDEX[6]), emission is observed at this wavelength even in ohmic plasmas, in our case having a total signal strength of the same order as that due to the charge-exchange recombination (CXR) emission. This ''passive'' emission is believed to be due to a combination of charge exchange from thermal neutrals with C^{6+} and electron-impact excitation of C^{5+}. The signals observed during ohmic plasmas are consistent with axisymmetric emission profiles. Both hollow and peaked emission profiles have been observed, with hollow profiles occurring most often.

Typical experimental spectra for five of the lines of sight are shown in Fig. 2, for both an Ohmic shot and an NBI-heated (but otherwise similar) shot. The figure also illustrates the instrument functions for each of the lines of sight.

A simulation of the CXR emission in a typical plasma is shown in Fig. 3 with the lines of sight overlaid. This simulation uses the beam-neutral density on the midplane as computed by a code (see below), and a C^{6+} density profile like those obtained from the fitting process described below. In typical START operating conditions ($T_e(0)\sim300-500$ eV, $n_e(0)\leqslant1\times10^{20}$ m^{-3}, $\tau_p\sim5$ ms), the fractional density of fully ionised carbon ions falls rapidly away from the plasma core,[7] in contrast to the situation in larger tokamaks. The beam profile accentuates this bias toward the core of the plasma where the beam is tangential. Also, the attenuation of the beam along its trajectory tends to localize the CXR emission toroidally. The result of these factors combined is that

[a)]Also at University of Essex, Wivenhoe Park, Colchester, UK.

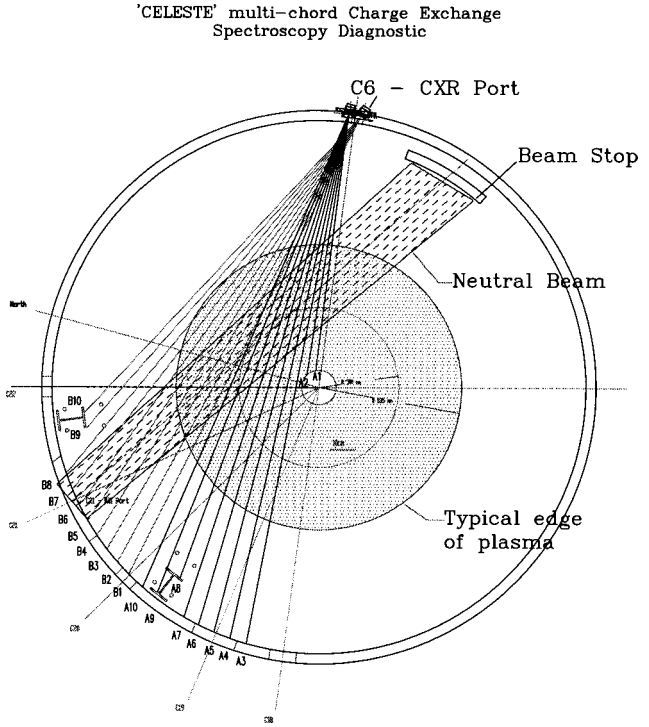

FIG. 1. Plan view of START midplane, showing lines of sight and NBI trajectory.

the CXR emission dominates the overall signal only for the central 4–6 lines of sight, with the other lines of sight collecting mostly passive emission (cf. Fig. 4).

The passive emission makes edge measurements possible. When the passive signals are combined with the CXR signals, $T_i(r)$ and $v_\phi(r)$ profiles can be determined over the full diameter of the plasma.

IV. ANALYSIS

The principal goal of the analysis for our present purposes is to unfold the set of spectra in terms of T_i and v_ϕ profiles and their associated errors.

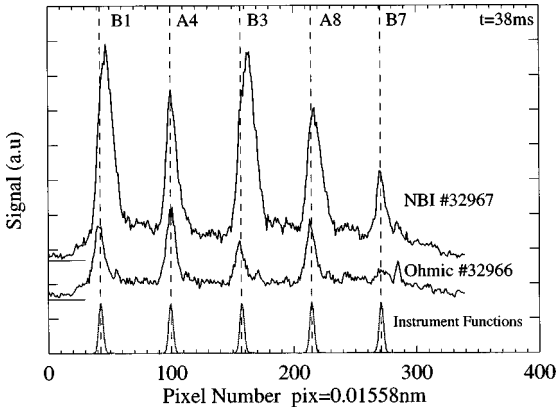

FIG. 2. Raw spectra with and without NBI, and instrument functions.

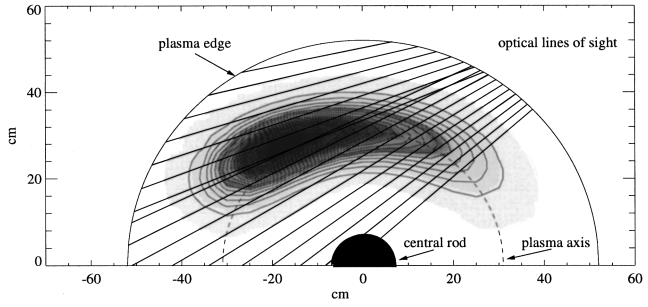

FIG. 3. Simulation of CXR emissivity.

A. Parametrizing the profiles

To perform a spatial inversion without making assumptions about the radial profiles would require a large number of lines of sight. Since the inboard region is only seen by lines of sight which also see the outboard region, signal quality would need to be excellent to prevent inward propagation of errors (this is inherent in any Abel-like inversion scheme). In addition, the absence of toroidal axisymmetry due to the CXR emission would necessitate the use of at least two distinct viewing locations for an unconstrained fit to be stable.

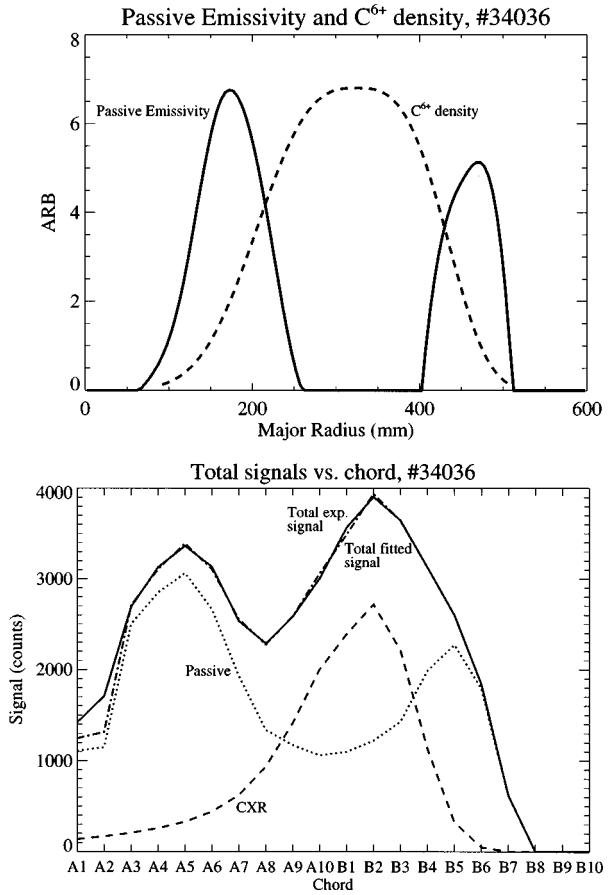

FIG. 4. Example of fitted profiles for C^{6+} density and passive emissivity, and associated total per-chord signals.

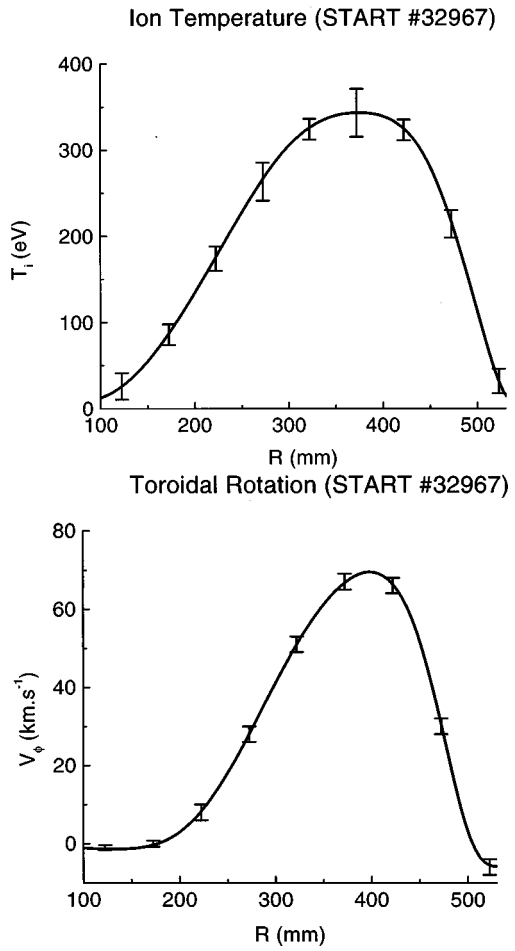

FIG. 5. Example of fitted profiles for T_i and v_ϕ, with error bars ($\pm 2\sigma$) estimated by Monte Carlo technique.

As the present setup on START consists of only 20 viewing chords at one toroidal location, some constraints on the radial profiles are unavoidable. The chosen constraints arise from a combination of physics assumptions and limits to the spatial frequencies that can realistically be attained.

The fitting algorithm fits four radial profiles to the spectra: T_i, v_ϕ, passive emissivity, and C^{6+} density. The constraints placed upon each are as follows:

(i) Temperature: assumed to be a flux-surface quantity. This is modeled as a 3–7 point profile with spline interpolation, with the number of points varying with data quality for a shot.

(ii) Velocity: the angular velocity is assumed to be a flux-surface quantity (hence the outward displacement of the linear velocity profile in Fig. 5). This is also modeled as a 3–7 point profile similarly to the temperature.

(iii) Passive emissivity: designated $\mathscr{E}_p$, this profile is modeled as an arbitrary function of major radius, typically using 10–14 points with spline interpolation. This profile is often observed to have very steep gradients, hence the requirement for a high spatial frequency in the fitting.

(iv) C^{6+} density: designated n_c, this is assumed to be a flux-surface quantity, and usually modeled as $n_c = n_c(0)e^{-|\rho/a_1|^{a_2}}$, where ρ is the flux-surface-corrected minor radius. This is the profile with the fewest degrees of freedom, because it is the least well resolved of the four. Results from STRAHL[7] runs using typical START parameters indicate that this functional form should be adequate.

Parametrizing the C^{6+} density profile presents the greatest physics uncertainties as it is not necessarily a flux surface quantity.[8–10] It has not been possible to let the density profile be unconstrained, because the data do not always distinguish sufficiently between passive and CXR emission. However, experience to date has shown that uncertainties in the precise mix of passive and active emission do not greatly alter the resulting fits for the profiles of T_i and v_ϕ, which are the main items of interest for the START physics investigations.

The flux-surface coordinates are obtained from equilibrium reconstruction using EFIT.[11]

B. Fitting algorithm

Having chosen the basis functions for each of the profiles, the next step is to search for the optimal set of coefficients. The chosen method is a nonlinear least-squares fit, using a variant of the gradient-descent algorithm due to Levenberg and Marquardt.[12]

Other methods exist for spatial inversion of line-integrated data, e.g., ''Abel-like'' linear inversion (as in Ref. 13); maximum entropy inversion.[14]

The use of a linear inversion method would in theory have been adequate. The zeroth, first, and second moments $M_{0,1,2}$ can be defined as follows for a spectrum S (where each S_i represents the signal in a detector channel):

$$M_0 = \sum_i S_i, \tag{1}$$

$$M_1 = \frac{1}{M_0} \sum_i i S_i, \tag{2}$$

$$M_2 = \frac{1}{M_0} \sum_i (i - M_1)^2 S_i, \tag{3}$$

with the moments corresponding to total signal, line centroid and the square of the linewidth, respectively. It is then straightforward to show that the second (or quadratic) moment of a composite spectrum (such as produced by a weighted sum of spectra from multiple zones within the plasma) is a linear combination of the zeroth, first, and second moments of the constituent spectra.

This allows the use of the second moment in a direct extension of the linear moment-inversion scheme described in Ref. 13 to handle not only ion velocities, but temperatures as well. However, tests have shown that the presence of even small amounts of noise in spectra causes the first and second moments to be significantly poorer estimators of line center and width respectively than a least-squares fit. This is most pronounced for the second moment, for which a factor of >5 in errors between the two methods was observed using synthetic spectra with signal strengths and detector noise similar to experimental values.

Such a method could still in principle have provided the starting point for a nonlinear iterative process (although a

quite different parametrization for the profiles would have been necessary). In practice, however, the occasional presence of other emission lines within the carbon spectra rendered it very difficult to measure accurately the moments of each spectrum, which are required by this method.

The maximum entropy approach is more difficult to implement, but would offer certain advantages, e.g., improved flexibility in the basis functions, and a more direct means of assessing uncertainties in fitted profiles. However, it would certainly be the most computationally expensive of the three methods.

The chosen method, least-squares fitting, explicitly takes account of uncertainties in signals and iterates to the most probable solution provided that the uncertainties have a Normal distribution (a condition which is adequately met for our data). In general, it is capable of reaching a stable solution with ten or fewer iterations.

Essentially, the fitting algorithm performs iterations of the following steps: (i) generate profiles, (ii) compute spectra arising from these profiles, (iii) compare these with the experimental spectra, (iv) modify coefficients for profiles using gradient descent algorithm.

The actual implementation of the algorithm has three phases. The first phase performs a fit for the n_c and $\mathscr{E}_p$ profiles only, primarily because this can be done without any knowledge of the shape of the spectrum, using only the total signal for each line of sight. The second phase holds the n_c and $\mathscr{E}_p$ profiles constant, and obtains best fits for T_i and v_ϕ using the full set of spectra. The third phase refines the fits for all four profiles. This final phase is necessary because of the difficulty in obtaining an accurate measurement of the total signal for lines of sight which have interfering emission lines. It is also useful because the shapes of the spectra hold extra information which can improve the quality of the n_c and $\mathscr{E}_p$ fit, even in the absence of such interference. This serves to break degeneracies that can exist between the n_c and $\mathscr{E}_p$ profiles when only total signal strength is taken into account.

The main advantage of using a three-phase algorithm is that it is much more efficient to search two (almost independent) subspaces than to search the full parameter space. Thus, the final phase begins with what is usually a close approximation to the optimal profiles, minimizing the number of iterations performed with all coefficients variable.

C. Computational details

Each complete iteration of the fit consists of the following (convergence criteria have been omitted for clarity):

(i) Generate the radial profiles from the coefficients.
(ii) Compute the resulting spectra, and the derivatives of the spectra with respect to each of the coefficients in the fit (for the $n_c/\mathscr{E}_p$ fit only the area under the spectrum is needed).
(iii) Compare experimental and computed spectra (compute χ^2).
(iv) Use the derivative information to take a step in coefficient space, dynamically resizing the step at each iteration to reduce χ^2. This stage involves recomputing the spectra (perhaps a number of times) but *not* the derivatives.

Profiles: Each of the profiles is generated on a finely spaced radial array, f_r, typically using 100 points across the diameter of the plasma. The spacing is chosen to be just small enough not to affect the fitting algorithm—gradually smaller spacings are used until the line-integrated spectra converge adequately with the fine-spacing limit. The profiles may thus be regarded as quasicontinuous.

The radial profiles are then remapped into a two-dimensional array, f_{jk}, where j denotes the line of sight and k denotes the position along the line of sight (same linear spacing as for radial array). This remapping uses a precomputed matrix to save time, and is necessary because the nonaxisymmetric CXR emission is not a function of radius.

Spectra: Next, the spectra are computed. The signal strength $S_j(\lambda_i)$ as a function of wavelength interval i (corresponding to the experimentally measured quantity, i.e., the signal in a detector channel) is computed as

$$S_j(\lambda_i)=\sum_k \left[\left(\mathscr{E}^p_{jk} + \sum_{l=1}^{\text{species}} q_l n^l_{jk} n^c_{jk} \right) \times \exp\{-[(\lambda_i-\lambda_0-\Delta\lambda^v_{jk})/\Delta\lambda^e_{jk}]^2\} \right], \tag{4}$$

where q_l is the charge-exchange rate coefficient for each of the four energy components of the beam (E_0, $E_0/2$, $E_0/3$, $E_0/20$, where E_0 is the primary beam energy, ~35 keV), n^l_{jk} is the computed neutral density for each beam component (see below), while $\Delta\lambda^v_{jk}$ and $\Delta\lambda^e_{jk}$ are related to the modeled velocity and temperature profiles as

$$T_i=\frac{m_i}{2k}\left(\frac{c\Delta\lambda_e}{\lambda_0}\right)^2, \quad V_\phi = c\,\frac{\Delta\lambda_v}{\lambda_0}. \tag{5}$$

This is by far the most computationally demanding stage of the algorithm. Much of the work goes into evaluating $\exp(-x^2)$ more than one hundred thousand times for the Gaussians at each iteration. Nearly all of the remaining computational time is spent calculating the derivatives when required (slightly less than half as often as spectra are computed). To improve accuracy and speed, an analytical form is used for the derivatives of the Gaussians, and these are then combined with numerical (forward difference) derivatives of the radial profiles. Using this technique means that computing both spectra and derivatives takes only two to three times longer than computing spectra alone. This is in contrast to the simplest technique (which was used in the developmental stages) of using numerical derivatives throughout, which takes $\sim(n_{\text{coeffs}}+1)$ times as long as computing the spectra, clearly much slower when n_{coeffs} can be 25 or higher.

Finally, all of the spectra and derivatives are convolved with the measured instrument function for each line of sight.

The calculation of n^l_{jk} in Eq. (4) above is made by a dedicated beam-modeling code,[5,15] using the T_e and n_e profiles from the Thomson scattering diagnostic.[3] This code models the attenuation of each of the nearly 2000 beamlets which form the beam, taking into account charge-exchange with both plasma and impurity ions, electron impact ioniza-

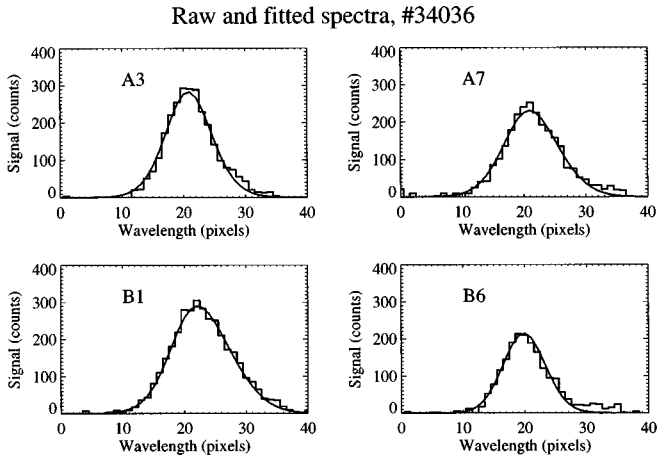

FIG. 6. Comparison of typical raw and fitted spectra.

tion, and ionization by plasma and impurity ions. The attenuation is mainly due to charge-exchange with the plasma ions.

Comparison: The comparison of the experimental and computed spectra is made by computing:

$$\chi^2=\sum_i \left(\frac{S_i^{\exp}-S_i^{\mathrm{comp}}}{\sigma_i}\right)^2, \tag{6}$$

where σ_i is the total rms error for the detector channel (i.e., a CCD pixel).

Results: The output from the fitting code for typical discharges is illustrated in Figs. 4–6. Profiles for n_c and $\mathscr{E}_p$ are shown in Fig. 4, along with the associated total signals for each chord with a breakdown of the contributions due to both sources of emission. Some fitted profiles for T_i and v_ϕ are shown in Fig. 5. Some examples of raw and fitted spectra are shown in Fig. 6.

V. ERROR ANALYSIS

There are many possible sources for errors in the final profiles for T_i and v_ϕ. There are random errors on the spectra themselves, due to both shot noise and detector (readout) noise. Inversion errors can be caused by imprecise calibration of the sensitivities and collection regions of the lines of sight. Other emission lines can also be present in the spectra, and these may not always be obvious (but when so, the affected pixels can be eliminated in the fitting code). Errors in the measurement of n_e and T_e will cause corresponding errors in the computed beam-neutral density which is used in the inversion process.

Further sources of error exist: ''difficult'' profiles which do not fit the chosen parameterisation may occur, or the fitting code may not find the global minimum of the χ^2 hypersurface.

The simplest errors to characterise are those due to the noise in the spectra, by the use of ''Monte Carlo'' techniques. Examples of such error estimates for the T_i and v_ϕ profiles can be seen in Fig. 5. The method of generating the error estimates is as follows: a sample set of the four profiles (fitted profiles from experimental data in this case) is used to generate a set of ideal (i.e., noiseless) spectra; these spectra are then used to generate many sets of synthetic (i.e., noisy) spectra, using Poisson deviates to model shot noise and Normal deviates to model the detector noise. The synthetic spectra are then analyzed as above. The errors in the computed radial profiles are then assessed to yield error bars as shown.

Errors due to most types of systematic problem are more difficult to assess. Sensitivity tests have been performed, on both real and simulated data, to assess the effects of most of these (e.g., calibration errors, ''difficult'' profiles). The results have indicated that many of the systematic errors quickly become apparent during the fitting process, with poor fits and high χ^2 values resulting. In the main, we find that the magnitude of the effect on the T_i and v_ϕ profiles at which systematic problems become evident is of the same order as the errors due to statistical noise.

Finally, there are the systematic errors due to atomic fine structure, and Zeeman and Stark splitting. The latter two are negligible on START due to the low magnetic and electrostatic fields. The main effect of the fine structure, if left uncorrected, would be to cause the calculated temperature to be slightly too high. For our conditions, this correction is roughly 10–20 eV depending on the actual temperature and density (which influence the l quantum-state mixing[16]).

ACKNOWLEDGMENTS

This work is jointly funded by the U.K. Department of Trade and Industry and EURATOM. The NBI equipment is on loan from Oak Ridge National Laboratory, U.S. The shipment of the NBI equipment was funded by the U.S. DOE. The EFIT code was provided by General Atomics, U.S.

[1] A. Sykes *et al.*, Plasma Phys. Controlled Fusion **39**, B247 (1997).
[2] P. G. Carolan *et al.*, Plasma Phys. Controlled Fusion **40**, 615 (1998).
[3] M. J. Walsh *et al.*, Proceedings of the 12th Topical Conference on High Temperature Plasma Diagnostics, 1998.
[4] P. G. Carolan *et al.*, Rev. Sci. Instrum. **68**, 1015 (1997).
[5] P. G. Carolan *et al.*, Plasma Phys. Rep. **24**, 206 (1998).
[6] P. G. Carolan *et al.*, Phys. Rev. A **35**, 3454 (1987).
[7] K. Behringer, Technical Report JET-R(87)08, JET, 1987.
[8] P. Helander, Phys. Plasmas **5**, 1209 (1998).
[9] P. Helander, Phys. Plasmas (to be published).
[10] J. Wesson, Nucl. Fusion **37**, 577 (1997).
[11] L. L. Lao *et al.*, Nucl. Fusion **25**, 1611 (1985).
[12] D. W. Marquardt, J. Soc. Ind. Appl. Math. **11**, 431 (1963).
[13] R. E. Bell, Rev. Sci. Instrum. **86**, 1273 (1997).
[14] E. T. Jaynes, *Maximum-Entropy and Bayesian Methods in Inverse Problems* (Reidel, Dordrecht, 1985).
[15] P. G. Carolan *et al.*, Proceedings of the 24th EPS Conference on Controlled Fusion and Plasma Physics, Part I (Berchtesgaden), 1997, p. 241.
[16] H. P. Summers, JET Report JET-IR(94)06, December 1994.